Computer Methods in Applied Mechanics and Engineering 459 (2026) 119083

Contents lists available at ScienceDirect

Comput. Methods Appl. Mech. Engrg.

journal homepage: www.elsevier.com/locate/cma

A variationally consistent model for wrinkling in hyperelastic membranes using spectral decomposition of the stress tensor

Daobo Zhang, Josef Kiendl *

Institute of Engineering Mechanics and Structural Analysis - University of the Bundeswehr Munich, Werner-Heisenberg-Weg 39, 85579, Neubiberg, Germany

ARTICLE INFO

Keywords:
Membrane
Wrinkling
Stress decomposition
Hyperelastic materials

ABSTRACT

We propose a variationally consistent and computationally efficient modeling approach for hyperelastic membranes undergoing wrinkling. Based on spectral decomposition of the stress tensor, the formulation enables a unified treatment of taut, wrinkled, and slack membrane states within a single expression, eliminating the need for case-specific logic. The plane stress condition is strictly enforced: analytically for incompressible materials and iteratively for compressible ones. The stress formulation builds upon the original hyperelastic stress and introduces a correction term governed mainly by the second principal stress, which yields a compact representation and enhances numerical efficiency. To assess the robustness and applicability of the proposed formulation, extensive numerical benchmark tests are conducted. The results confirm its strong predictive capability and suitability for implementation in both standard finite element and isogeometric analysis frameworks.

1. Introduction

Membrane structures are prone to wrinkling, which is characterized by localized out-of-plane deformation, as they can hardly withstand any compressive stress. Since this phenomenon significantly affects the mechanical performance and stability of structures, it has attracted considerable attention across aerospace, marine, biomedical, and flexible electronic applications. Due to its localized and highly nonlinear nature, the modeling and prediction of wrinkling are still evolving, driven by growing interest in a broader range of material models.

Various approaches have been developed to characterize the mechanical behavior of wrinkled membranes, all of which are based on two fundamental frameworks: plate and shell theory, and tension-field theory (TFT). These two frameworks differ in their theoretical assumptions, computational cost, resolution capabilities, and practical applicability.

Plate and shell theory-based models incorporate both membrane and bending stiffness, enabling explicit characterization of wrinkle morphology, including wavelength and amplitude. In practice, achieving accurate results often demands dense meshes and incurs high computational cost. The evolution of such models generally follows an increasing order of geometric nonlinearity. The classical Föppl–von Kármán (FvK) plate model [1,2], based on small in-plane strains and linearized curvature, was later extended to the extended FvK (EFvK) model [3] to account for finite in-plane strains. Further developments include the Kirchhoff–Love (KL) shell theory [4], which extends the applicability to curved geometries while still employing linearized curvature, and Koiter's plate theorys [5–7], which adopts a higher-order curvature representation. More recently, the consistent finite-strain plate model [8] has been proposed to achieve asymptotic consistency with three-dimensional elasticity without relying on a priori kinematic assumptions.

* Corresponding author.
E-mail address: josef.kiendl@unibw.de (J. Kiendl).

https://doi.org/10.1016/j.cma.2026.119083
Received 5 February 2026; Received in revised form 2 April 2026; Accepted 13 May 2026
Available online 20 May 2026
0045-7825/© 2026 The Authors. Published by Elsevier B.V. This is an open access article under the CC BY license (http://creativecommons.org/licenses/by/4.0/).

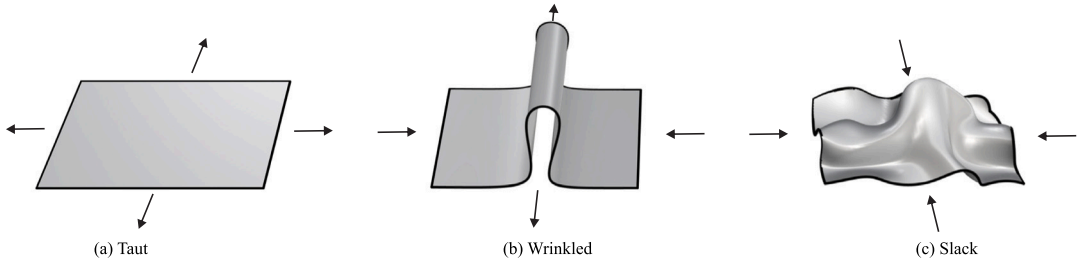

Fig. 1. Membrane regions classified as (a) taut, (b) wrinkled, (c) slack [20].

These models, and their subsequent extensions to hyperelastic [9–11], orthotropic [12,13], and anisotropic [14,15] materials, have been widely applied to capture wrinkling behavior in membranes. However, as an alternative numerical modeling approach, methods based on tension-field theory (TFT) [16] provide a simplified framework that neglects bending stiffness and assumes a uniaxial tension state in wrinkled regions, where the compressive stress along the wrinkle direction vanishes. Despite their potential, numerical models based on TFT for hyperelastic materials have been rarely reported in the literature.

In numerical applications, a coarse membrane mesh with wrinkling models based on TFT is sufficient for capturing accurate stress and displacement fields, while providing wrinkle orientations and classifying membrane regions as taut, wrinkled, or slack (as shown in Fig. 1), according to a wrinkling criterion based on principal stress, strain, or both [17,18], see Fig. 4. The advantages and limitations of these criteria have been discussed in previous studies [19,20], and the mixed criterion is generally regarded as the most effective one.

However, due to the absence of bending stiffness, these models cannot reproduce detailed wrinkle geometry. Nevertheless, they are widely used in large-scale membrane simulations [21–23] because of their computational efficiency.

Wrinkling models based on TFT are commonly divided into two categories, which modify either the kinematics or the constitutive law so that the compressive stress along the wrinkle direction vanishes [21,24]. Comprehensive discussions of these approaches are provided in [21,24]. Representative approaches of kinematic modification methods include the incorporation of virtual elongation or shear components into the deformation gradient [21,25], saturation-based strain adjustment [26], and direct strain modification [27]. Material modification methods comprise iterative updates of the material matrix [28], penalization and projection techniques [18,24,29–34], relaxed strain–energy formulations [35], and more recent variationally consistent spectral-decomposition models [19,20].

As discussed earlier, numerical models based on these methods have mostly been limited to linear elasticity, with only a few studies addressing wrinkled hyperelastic membranes. Some attempts have been reported, such as the work by [36,37], but this approach does not account for compressible behavior. More recently, [38] extended the model proposed by [17] to the hyperelastic regime. However, the use of conditional logic linked to a wrinkling criterion diminishes convergence robustness, while the additional root-finding step for determining the wrinkle direction at each quadrature point increases computational expense.

In this paper, we propose a variationally consistent and computationally efficient wrinkling model for hyperelastic membranes, based on the spectral decomposition of the stress tensor. The proposed model enables the unified treatment of taut, wrinkled, and slack membrane states within a single expression, eliminating the need for case-specific logic or switching criteria. The formulation is general and supports arbitrary three-dimensional constitutive laws, allowing both compressible and incompressible hyperelastic materials to be incorporated into the analysis. The plane stress condition is enforced to eliminate the transverse normal stress, with different treatment strategies for compressible and incompressible materials: for compressible models, the transverse stretch is computed iteratively, whereas for incompressible cases, it is resolved analytically via the incompressibility constraint.

The paper is organized as follows. Section 2 presents the membrane formulations for general hyperelastic materials, covering the geometry, kinematics, and constitutive law. Section 3 introduces a new wrinkling model based on the spectral decomposition of the stress tensor to accommodate hyperelastic materials. Section 4 describes the variational formulation based on the principle of virtual work and outlines the isogeometric discretization strategy used in the implementation. To demonstrate the effectiveness and applicability of the proposed approach, Section 5 provides several numerical examples, including comparisons with experimental and shell-based reference solutions. Finally, Section 6 summarizes the main findings and discusses possible directions for future research.

2. Membrane formulations for general hyperelastic materials

This section presents the geometric description, kinematic framework, and constitutive formulation for hyperelastic membranes. As illustrated in Fig. 2, the membrane is modeled as a curved surface with thickness t, and its position in the deformed configuration is described by the vector field $\mathbf{x}(\theta^\alpha)$. The parameters θ^α represent the surface coordinates, where Greek indices range over $\{1,2\}$, and the Einstein summation convention is assumed for repeated indices. The covariant base vectors on the current midsurface are given by:

$$\mathbf{g}_\alpha = \frac{\partial \mathbf{x}}{\partial \theta^\alpha} = \mathbf{x}_{,\alpha}. \tag{1}$$

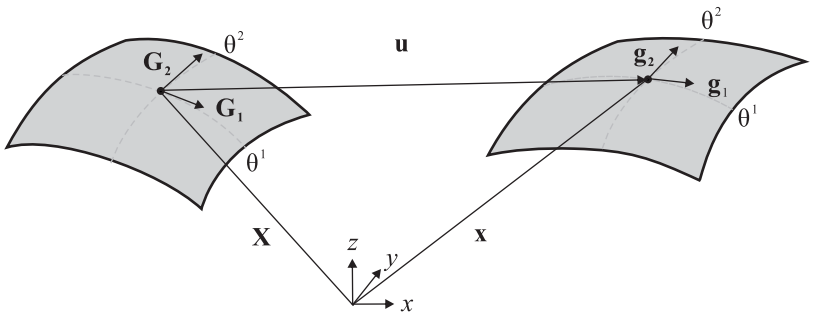

Fig. 2. A representative schematic of the membrane geometry [19], showing the midsurface positions **X** and **x** in the undeformed and deformed states, with displacement **u**.

In the undeformed (reference) configuration, the corresponding covariant base vectors are denoted $\mathbf{G}_\alpha$. The associated contravariant vectors $\mathbf{G}^\alpha$ and $\mathbf{g}^\alpha$ are defined such that:

$$\mathbf{G}^\alpha \cdot \mathbf{G}_\beta = \delta^\alpha_\beta, \quad \mathbf{g}^\alpha \cdot \mathbf{g}_\beta = \delta^\alpha_\beta, \tag{2}$$

where δ^α_β is the Kronecker delta, which equals 1 when $\alpha = \beta$ and 0 otherwise. The surface metric tensors for the reference and current configurations are given by:

$$G_{\alpha\beta} = \mathbf{G}_\alpha \cdot \mathbf{G}_\beta, \quad g_{\alpha\beta} = \mathbf{g}_\alpha \cdot \mathbf{g}_\beta. \tag{3}$$

In addition, the base vectors $\mathbf{G}_1$ and $\mathbf{G}_2$ can also be used to define a local Cartesian basis, together with the corresponding coordinates $\hat{\theta}^1$ and $\hat{\theta}^2$:

$$\mathbf{E}_1 = \frac{\mathbf{G}_1}{\|\mathbf{G}_1\|}, \quad \mathbf{E}_2 = \frac{\mathbf{G}_2 - (\mathbf{G}_2 \cdot \mathbf{E}_1)\mathbf{E}_1}{\left\|\mathbf{G}_2 - (\mathbf{G}_2 \cdot \mathbf{E}_1)\mathbf{E}_1\right\|}. \tag{4}$$

The deformation gradient $\mathbf{F}$ is constructed as:

$$\mathbf{F} = \mathbf{g}_\alpha \otimes \mathbf{G}^\alpha, \quad \mathbf{F}^T = \mathbf{G}^\alpha \otimes \mathbf{g}_\alpha. \tag{5}$$

Based on this, the right Cauchy–Green deformation tensor $\mathbf{C}$ takes the form:

$$\mathbf{C} = \mathbf{F}^T\mathbf{F} = g_{\alpha\beta}\mathbf{G}^\alpha \otimes \mathbf{G}^\beta. \tag{6}$$

To characterize the nonlinear strain behavior, the Green–Lagrange strain tensor $\mathbf{E}$ is adopted and defined as:

$$\mathbf{E} = \frac{1}{2}\left(\mathbf{F}^T\mathbf{F} - \mathbf{I}\right) = \frac{1}{2}\left(\mathbf{C} - \mathbf{I}\right) = E_{\alpha\beta}\mathbf{G}^\alpha \otimes \mathbf{G}^\beta, \tag{7}$$

where $\mathbf{I}$ is the second-order identity tensor. The in-plane strain components are specifically given by:

$$E_{\alpha\beta} = \frac{1}{2}\left(g_{\alpha\beta} - G_{\alpha\beta}\right). \tag{8}$$

To capture the three-dimensional material response within this framework, a suitable constitutive model is required. [4] presents a consistent and general derivation of an arbitrary isotropic hyperelastic model with the strain energy function $\psi(\mathbf{C})$, which transitions from a 3D continuum to a shell model applicable to both compressible and incompressible materials. This approach also applies to membrane formulations.

As the energetically conjugate quantity to the Green–Lagrange strain tensor $\mathbf{E}$, the second Piola–Kirchhoff 3D stress tensor, $\mathbf{S} = S^{ij}\mathbf{G}_i \otimes \mathbf{G}_j$, is used:

$$S^{ij} = \frac{\partial \psi}{\partial E_{ij}} = 2\frac{\partial \psi}{\partial C_{ij}}, \tag{9}$$

where Latin indices take on values $\{1, 2, 3\}$. Then, the corresponding tangent material tensor, $\mathbb{C} = \mathbb{C}^{ijkl}\mathbf{G}_i \otimes \mathbf{G}_j \otimes \mathbf{G}_k \otimes \mathbf{G}_l$, is given by:

$$\mathbb{C}^{ijkl} = \frac{\partial^2 \psi}{\partial E_{ij}\partial E_{kl}} = 4\frac{\partial^2 \psi}{\partial C_{ij}\partial C_{kl}}. \tag{10}$$

However, when adopting the assumption $C_{33} = g_{33} = 1$ for the membrane model, the plane stress condition is generally not satisfied as $S^{33} = 2\partial\psi/\partial C_{33} \neq 0$. To ensure that $S^{33} = 0$, the transverse normal component C_{33} must be determined. Once the plane stress condition is enforced, the transverse strain E_{33} can be eliminated via static condensation, leading to:

$$S^{33} = \mathbb{C}^{33\alpha\beta}E_{\alpha\beta} + \mathbb{C}^{3333}E_{33} = 0, \tag{11}$$

which further gives:

$$E_{33} = -\frac{\mathbb{C}^{33\alpha\beta}}{\mathbb{C}^{3333}} E_{\alpha\beta}. \tag{12}$$

Substituting this result into the material tensor yields the statically condensed form:

$$\hat{\mathbb{C}}^{\alpha\beta\gamma\delta} = \mathbb{C}^{\alpha\beta\gamma\delta} - \frac{\mathbb{C}^{\alpha\beta33}\mathbb{C}^{33\gamma\delta}}{\mathbb{C}^{3333}}. \tag{13}$$

For incompressible materials, this can be done analytically as the strain energy function is augmented by a constraint term that enforces the Jacobian determinant $J = \det(\mathbf{F}) = 1$ using a Lagrange multiplier p, which represents the hydrostatic pressure:

$$\psi = \psi_{el}(\mathbf{C}) - p(J-1). \tag{14}$$

By eliminating p through the plane stress condition and substituting the incompressibility condition into the 3D stress tensor, the in-plane components of the stress tensor for the membrane formulation is obtained as:

$$S^{\alpha\beta} = 2\frac{\partial\psi_{el}}{\partial C_{\alpha\beta}} - 2\frac{\partial\psi_{el}}{\partial C_{33}} J_0^{-2} g^{\alpha\beta}, \tag{15}$$

with the in-plane Jacobian determinant $J_0 = \sqrt{|g_{\alpha\beta}|/|G_{\alpha\beta}|}$, and the contravariant metric coefficients $g^{\alpha\beta}$ can be obtained by the inverse matrix of the covariant coefficients, i.e., $[g^{\alpha\beta}] = [g_{\alpha\beta}]^{-1}$. Accordingly, the statically condensed material tensor takes the form:

$$\begin{aligned}\hat{\mathbb{C}}^{\alpha\beta\gamma\delta} = {} & 4\frac{\partial^2\psi_{el}}{\partial C_{\alpha\beta}\partial C_{\gamma\delta}} + 4\frac{\partial^2\psi_{el}}{\partial C_{33}^2} J_0^{-4} g^{\alpha\beta} g^{\gamma\delta} - 4\frac{\partial^2\psi_{el}}{\partial C_{33}\partial C_{\alpha\beta}} J_0^{-2} g^{\gamma\delta} - 4\frac{\partial^2\psi_{el}}{\partial C_{33}\partial C_{\gamma\delta}} J_0^{-2} g^{\alpha\beta} \\ & + 2\frac{\partial\psi_{el}}{\partial C_{33}} J_0^{-2}\left(2g^{\alpha\beta}g^{\gamma\delta} + g^{\alpha\gamma}g^{\beta\delta} + g^{\alpha\delta}g^{\beta\gamma}\right).\end{aligned} \tag{16}$$

For compressible materials, however, the plane stress condition $S^{33} = 0$ is enforced by iteratively solving for C_{33} locally at the integration point. The plane stress condition can be linearized using the Newton method:

$$S^{33} + \frac{\partial S^{33}}{\partial C_{33}} \Delta C_{33} = S^{33} + \frac{1}{2}\mathbb{C}^{3333}\Delta C_{33} = 0. \tag{17}$$

From this, the incremental correction ΔC_{33} at iteration step I is obtained as:

$$\Delta C_{33}^{(I)} = -2\frac{S_{(I)}^{33}}{\mathbb{C}_{(I)}^{3333}}, \tag{18}$$

and the updated C_{33} for the next iteration is:

$$C_{33}^{(I+1)} = C_{33}^{(I)} + \Delta C_{33}^{(I)}. \tag{19}$$

At each iteration, $\mathbf{C}$, $\mathbf{S}(\mathbf{C})$, and $\mathbb{C}(\mathbf{C})$ are updated until convergence. Once the Eq. (17) is met within a specified tolerance, the statically condensed material tensor $\hat{\mathbb{C}}^{\alpha\beta\gamma\delta}$ is obtained using Eq. (13), ensuring that only the in-plane stress components $S^{\alpha\beta}$ and $\hat{\mathbb{C}}^{\alpha\beta\gamma\delta}$ are retained in the membrane formulation.

3. Wrinkling model based on spectral decomposition of the stress tensor for hyperelastic materials

In this section, we present an efficient formulation of the wrinkling model for isotropic hyperelastic materials using spectral decomposition of the stress tensor. It is constructed based on the uniaxial tension condition derived from classical tension-field theory. This condition assumes that, in the wrinkled state, the stress along the wrinkle direction is completely released. As shown in Fig. 3, three different configurations are introduced. In the current configuration, the wrinkled membrane surface, which becomes geometrically flattened in the fictitious configuration, is depicted by solid lines, while the pseudo mean surface, represented by a rectangular plane of length L, is shown with dashed lines.

The vectors $\mathbf{w}$ and $\tilde{\mathbf{w}}$ represent the nominal and modified vectors indicating wrinkling directions in the current and fictitious configurations, respectively. $\mathbf{F}$ is the standard deformation gradient associated with the actual deformation from the reference configuration, and $\tilde{\mathbf{F}}$ represents the modified deformation gradient incorporating the fictitious flattening of wrinkles and is defined according to [25] as follows

$$\tilde{\mathbf{F}} = \bar{\mathbf{F}}\mathbf{F} = (\mathbf{I} + \beta\mathbf{w}\otimes\mathbf{w})\mathbf{F}. \tag{20}$$

The scalar β characterizes the amount of the elongation of the pseudo mean surface. In addition, the vectors $\mathbf{t}$, and $\tilde{\mathbf{t}}$ denote the corresponding in-plane directions perpendicular to $\mathbf{w}$, and $\tilde{\mathbf{w}}$, respectively.

By substituting the modified deformation gradient tensor $\tilde{\mathbf{F}}$ into Eq. (7), the original Green–Lagrange strain tensor $\mathbf{E}$ is modified as

$$\tilde{\mathbf{E}} = \frac{1}{2}(\tilde{\mathbf{F}}^T\tilde{\mathbf{F}} - \mathbf{I}) = \mathbf{E} + \frac{1}{2}\beta(\beta+2)\mathbf{w}_0\otimes\mathbf{w}_0, \tag{21}$$

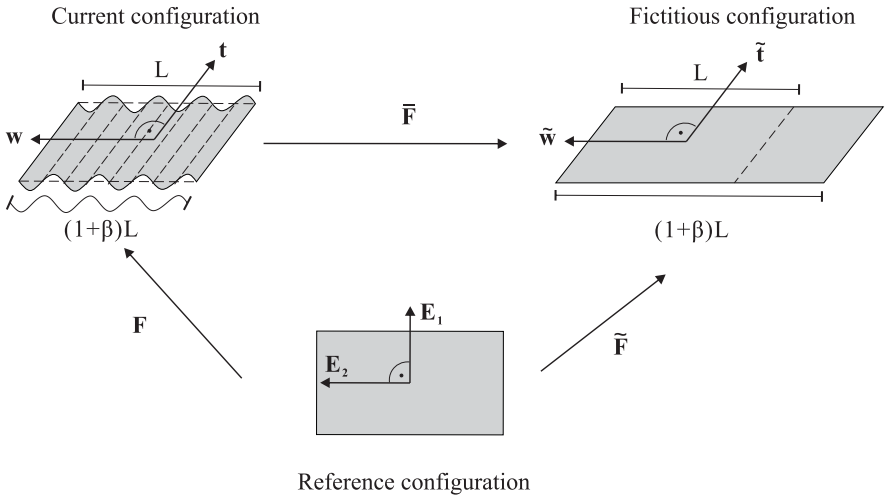

Fig. 3. Transformations among the various configurations of a membrane.

with $\mathbf{w}_0$ introduced as

$$\mathbf{w}_0 = \mathbf{F}^{\mathrm{T}}\mathbf{w}. \tag{22}$$

Note that $\mathbf{w}_0$ does not represent the wrinkling direction in the reference configuration, i.e. it is not the pull-back of $\mathbf{w}$, further details can be found in [24]. Correspondingly, the second Piola–Kirchhoff stress tensor $\mathbf{S}$ is also modified as $\tilde{\mathbf{S}}$, representing the modified stress state after wrinkling. Their explicit expressions will be provided later. According to the uniaxial tension condition, the stress in the wrinkling direction must vanish. Mathematically, it is written as:

$$\tilde{\boldsymbol{\sigma}}\tilde{\mathbf{w}} = \mathbf{0}. \tag{23}$$

This condition is equivalent to:

$$\tilde{\mathbf{w}} \cdot \tilde{\boldsymbol{\sigma}}\tilde{\mathbf{w}} = 0, \quad \tilde{\mathbf{t}} \cdot \tilde{\boldsymbol{\sigma}}\tilde{\mathbf{w}} = 0. \tag{24}$$

In this expression, the first and second conditions mean that the normal and shear stress component along the wrinkling direction vanish in the wrinkled region. The associated modified Cauchy stress tensor $\tilde{\boldsymbol{\sigma}}$ in the fictitious configuration can be obtained from $\tilde{\mathbf{S}}$ through the push-forward relation:

$$\tilde{\boldsymbol{\sigma}} = \frac{1}{\det\tilde{\mathbf{F}}}\,\tilde{\mathbf{F}}\tilde{\mathbf{S}}\tilde{\mathbf{F}}^{\mathrm{T}}. \tag{25}$$

Then, the first conditions described above can be reformulated in terms of the modified PK2 stress tensor $\tilde{\mathbf{S}}$ as follows:

$$\mathbf{w}_0 \cdot \tilde{\mathbf{S}}\mathbf{w}_0 = \tilde{\mathbf{S}} : \mathbf{w}_0 \otimes \mathbf{w}_0 = 0. \tag{26}$$

In isotropic materials, where the direction of $\mathbf{w}_0$ coincides with the direction of the second principal stress, spectral decomposition of the original stress tensor $\mathbf{S}$ can be employed to identify the wrinkling direction:

$$\mathbf{S} = S_\alpha \mathbf{N}_\alpha \otimes \mathbf{N}_\alpha = S_\alpha \mathbf{M}_\alpha, \tag{27}$$

where S_α are the principal stresses, ordered such that $S_1 \geq S_2$, and $\mathbf{N}_\alpha$ are the associated principal directions. A second-order tensor $\mathbf{M}_2$ is introduced to characterize the direction associated with $\mathbf{w}_0$. The modified strain tensor $\tilde{\mathbf{E}}$ is given below, and the corresponding stress tensor $\tilde{\mathbf{S}}$ is obtained using the original material tensor $\mathbb{C}$ as follows:

$$\tilde{\mathbf{E}} = \mathbf{E} + \mu_w \mathbf{M}_2, \quad \tilde{\mathbf{S}} = \mathbb{C} : \tilde{\mathbf{E}}, \tag{28}$$

where μ_w represents the magnitude of wrinkling. Its value follows from enforcing the uniaxial tension condition Eq. (26). Substituting Eq. (28) into this condition gives:

$$\mathbb{C} : \left(\mathbf{E} + \mu_w \mathbf{M}_2\right) : (\mathbf{w}_0 \otimes \mathbf{w}_0) = \left(\mathbf{S} + \mu_w\, \mathbb{C} : \mathbf{M}_2\right) : \mathbf{M}_2 = 0. \tag{29}$$

Solving for μ_w yields

$$\mu_w = -\frac{\mathbf{M}_2 : \mathbf{S}}{\mathbf{M}_2 : \mathbb{C} : \mathbf{M}_2}. \tag{30}$$

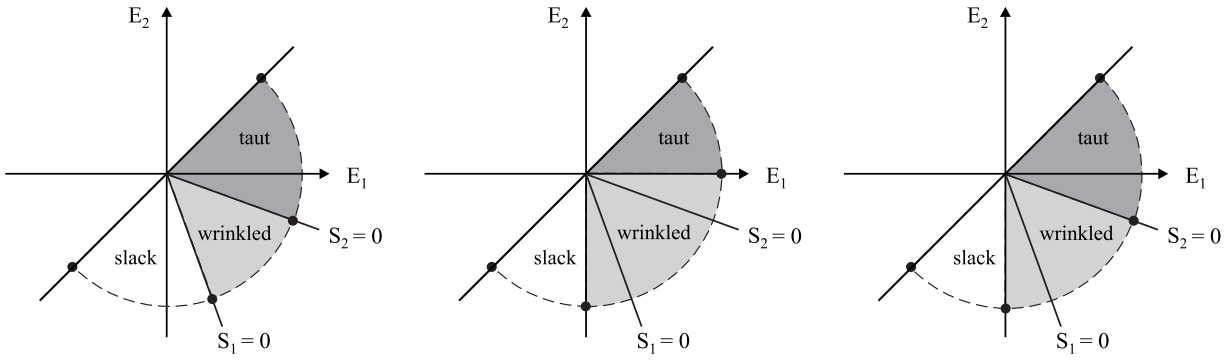

(a) Principal stress criterion (b) Principal strain criterion (c) Mixed criterion

Fig. 4. Different wrinkling criteria.

Note that $\mathbf{M}_2$ is expressed in the principal basis (i.e., along the eigenvectors), a transformation between the curvilinear and principal coordinate systems is required and can be found in [39]. Accordingly, the modified strain tensor in Eq. (28) can be rewritten as:

$$\tilde{\mathbf{E}} = \left(\mathbb{I} - \frac{1}{\mathbf{M}_2 : \mathbb{C} : \mathbf{M}_2} \left(\mathbb{C} : \mathbf{M}_2 \right) \otimes \mathbf{M}_2 \right) : \mathbf{E} = \mathbb{B} : \mathbf{E}, \tag{31}$$

where $\mathbb{I}$ is the fourth-order identity tensor. Here, the fourth-order operator $\mathbb{B}$ acts as a projection tensor that removes the strain components producing stress in the wrinkle direction $\mathbf{M}_2$. In other words, $\mathbb{B}$ projects the total strain $\mathbf{E}$ onto the subspace in which the stress along the wrinkle direction vanishes. Consequently, the modified stress tensor takes the form:

$$\tilde{\mathbf{S}} = \left(\mathbb{I} - \frac{1}{\mathbf{M}_2 : \mathbb{C} : \mathbf{M}_2} \left(\mathbb{C} : \mathbf{M}_2 \right) \otimes \mathbf{M}_2 \right) : \mathbf{S} = \mathbb{B} : \mathbf{S}. \tag{32}$$

By substituting the spectral form of the stress tensor into the modified formulation, the expression for $\tilde{\mathbf{S}}$ becomes:

$$\tilde{\mathbf{S}} = \left(\mathbb{I} - \frac{1}{\mathbf{M}_2 : \mathbb{C} : \mathbf{M}_2} \left(\mathbb{C} : \mathbf{M}_2 \right) \otimes \mathbf{M}_2 \right) : \left(S_1 \mathbf{M}_1 + S_2 \mathbf{M}_2 \right) \tag{33}$$

Due to the orthogonality of the principal directions, i.e., $\mathbf{M}_\alpha : \mathbf{M}_\beta = \delta_{\alpha\beta}$, this leads to a simplified expression for the modified stress:

$$\tilde{\mathbf{S}} = S_1 \mathbf{M}_1 + S_2 \mathbf{M}_2 + \frac{-S_2}{\mathbf{M}_2 : \mathbb{C} : \mathbf{M}_2} \mathbb{C} : \mathbf{M}_2. \tag{34}$$

Note that this stress expression is only for the wrinkled state. As seen in the expression, the sum of the first two terms recovers the original stress tensor $\mathbf{S}$.

Furthermore, in order to represent the three distinct membrane states, namely taut, wrinkled, and slack, in a unified manner within a single formulation, we follow the variationally consistent approach proposed in [19], along with the mixed wrinkling criterion. Accordingly, the modified stress tensor in Eq. (34) is decomposed into its positive and negative parts as:

$$\mathbf{S}^{\pm} = H^{\pm}\left(E_1\right) \mathbf{S} \pm \left(H^{-}\left(S_2\right) H^{+}\left(E_1\right) \right) \frac{-S_2}{\mathbf{M}_2 : \mathbb{C} : \mathbf{M}_2} \mathbb{C} : \mathbf{M}_2, \tag{35}$$

where $H^{\pm}(x)$ represents the ramp function, defined as $H^{+}(x) = (x + |x|)/2x$ and $H^{-}(x) = 1 - H^{+}(x)$. Therefore, this decomposition satisfies the mixed criterion, as illustrated in Fig. 4. Specifically, when $S_2 > 0$, both principal stress components are positive, i.e., the membrane is in the taut state, and $\mathbf{S}$ lies entirely in the positive part defined by the present split. When $E_1 > 0$ and $S_2 \leq 0$, the membrane is classified as wrinkled. In this regime, the second term in Eq. (35) becomes active, modifying the stress state according to the proposed decomposition. Finally, when $E_1 \leq 0$, the membrane is in the slack state, and $\mathbf{S}$ lies entirely in the negative part defined by the present split. This formulation avoids the premature transition to the slack state predicted by the principal stress criterion when $S_1 \leq 0$, as well as the inaccurate early onset of the wrinkled state induced by the principal strain criterion when $E_2 \leq 0$.

Consequently, the positive and negative material tensors can be obtained by deriving the corresponding stress tensors with respect to the Cauchy deformation tensor $\mathbf{C}$:

$$\mathbb{C}^{\pm} = 2\frac{\partial \mathbf{S}^{\pm}}{\partial \mathbf{C}} = H^{\pm}\left(E_1\right) \mathbb{C} \pm \left(H^{-}\left(S_2\right) H^{+}\left(E_1\right) \right) \left(2\frac{\partial S_2}{\partial \mathbf{C}} \otimes \left(\frac{-1}{\mathbf{M}_2 : \mathbb{C} : \mathbf{M}_2} \mathbb{C} : \mathbf{M}_2 \right) + 2S_2 \frac{\partial \left(\frac{-1}{\mathbf{M}_2 : \mathbb{C} : \mathbf{M}_2} \mathbb{C} : \mathbf{M}_2 \right)}{\partial \mathbf{C}} \right). \tag{36}$$

The derivatives of the last term can be written as:

$$\frac{\partial\left(\frac{-1}{\mathbf{M}_2:\mathbb{C}:\mathbf{M}_2}\mathbb{C}:\mathbf{M}_2\right)}{\partial\mathbf{C}} = -\left(\frac{\partial\left(\frac{1}{\mathbf{M}_2:\mathbb{C}:\mathbf{M}_2}\right)}{\partial\mathbf{C}}\otimes(\mathbb{C}:\mathbf{M}_2)+\frac{1}{\mathbf{M}_2:\mathbb{C}:\mathbf{M}_2}\frac{\partial\mathbb{C}}{\partial\mathbf{C}}:\mathbf{M}_2+\frac{1}{\mathbf{M}_2:\mathbb{C}:\mathbf{M}_2}\mathbb{C}:\frac{\partial\mathbf{M}_2}{\partial\mathbf{C}}\right), \tag{37}$$

where the derivative of the first term can be represented as:

$$\frac{\partial\left(\frac{1}{\mathbf{M}_2:\mathbb{C}:\mathbf{M}_2}\right)}{\partial\mathbf{C}} = \frac{-\frac{\partial(\mathbf{M}_2:\mathbb{C}:\mathbf{M}_2)}{\partial\mathbf{C}}}{(\mathbf{M}_2:\mathbb{C}:\mathbf{M}_2)^2} = -\left(\frac{\frac{\partial\mathbf{M}_2}{\partial\mathbf{C}}:\mathbb{C}:\mathbf{M}_2+\mathbf{M}_2:\frac{\partial\mathbb{C}}{\partial\mathbf{C}}:\mathbf{M}_2+\mathbf{M}_2:\mathbb{C}:\frac{\partial\mathbf{M}_2}{\partial\mathbf{C}}}{(\mathbf{M}_2:\mathbb{C}:\mathbf{M}_2)^2}\right). \tag{38}$$

As can be seen from the expressions, the necessary derivatives with respect to the Cauchy deformation tensor $\mathbf{C}$, including $\partial S_2/\partial\mathbf{C}$, $\partial\mathbf{M}_2/\partial\mathbf{C}$, and $\partial\mathbb{C}/\partial\mathbf{C}$ are required. Detailed evaluations of these derivatives are provided in Appendix B.

To suppress unphysical compressive or negative stresses, the stress and material tangent tensors are modified by retaining only their positive components. The resulting formulation reads:

$$\mathbf{S}_{\text{eff}} = \mathbf{S}^+, \quad \mathbb{C}_{\text{eff}} = \mathbb{C}^+. \tag{39}$$

Alternatively, as discussed in [21,24,33,40], it is argued that membranes may still exhibit residual compressive stiffness even in the wrinkled state. To accommodate this observation, we generalize the model by introducing a degradation factor $\eta \ll 1$, which allows a small fraction of compressive stress to remain. The modified stress and material tensors are then defined as:

$$\mathbf{S}_{\text{eff}} = \mathbf{S}^+ + \eta\mathbf{S}^-, \quad \mathbb{C}_{\text{eff}} = \mathbb{C}^+ + \eta\mathbb{C}^-. \tag{40}$$

Further details for this regularized formulation can be found in [19]. The strain energy density can also be expressed in an additive form incorporating the degradation factor and can be obtained by integrating the stress with respect to the strain; however, the detailed derivation is omitted here for brevity.

Remark 1. In the case of a St. Venant–Kirchhoff material under plane stress, the sum of the terms involving $\mathbf{M}_2$ in the Eq. (34) can be further simplified. Specifically, we have:

$$S_2\mathbf{M}_2 + \frac{-S_2}{\mathbf{M}_2:\mathbb{C}:\mathbf{M}_2}\mathbb{C}:\mathbf{M}_2 = -\nu S_2\mathbf{M}_1, \tag{41}$$

where ν denotes Poisson's ratio and the proof can be found in Appendix A. As a result, the modified stress tensor under plane stress reduces to the form:

$$\tilde{\mathbf{S}} = S_1\mathbf{M}_1 - \nu S_2\mathbf{M}_1, \tag{42}$$

which is equivalent to the representation proposed in [19]:

$$\tilde{\mathbf{S}} = EE_1\mathbf{M}_1, \tag{43}$$

where the principal stresses are related to the principal strains by:

$$S_1 = \frac{E}{1-\nu^2}\left(E_1+\nu E_2\right), \quad S_2 = \frac{E}{1-\nu^2}\left(E_2+\nu E_1\right). \tag{44}$$

Here, E is Young's modulus and E_α denotes the principal strains, assuming $E_1 \geq E_2$.

4. Variational formulation and isogeometric discretization

The starting point is the principle of virtual work, which states that the system is in equilibrium if the internal virtual work balances the external virtual work for any admissible virtual displacement $\delta\mathbf{u}$:

$$\delta W(\mathbf{u},\delta\mathbf{u}) = \delta W^{\text{int}} - \delta W^{\text{ext}} = 0. \tag{45}$$

Here, δW^{int} and δW^{ext} denote the internal and external virtual work, respectively. For membrane structures, the virtual internal work is expressed in terms of the effective second Piola–Kirchhoff stress tensor $\mathbf{S}_{\text{eff}}$ and the virtual Green–Lagrange strain tensor $\delta\mathbf{E}$, while external work is expressed in terms of applied forces $\mathbf{f}$ and the virtual displacement $\delta\mathbf{u}$. Since the membrane is thin, its deformation is assumed to be constant through the thickness. Thus, the differential volume is approximated by $dV \approx t\,dA$, where t is the membrane thickness and dA is the differential area on the midsurface. Accordingly, the virtual work expression becomes:

$$\delta W(\mathbf{u},\delta\mathbf{u}) = \delta W^{\text{int}} - \delta W^{\text{ext}} = \int_A \mathbf{S}_{\text{eff}} : \delta\mathbf{E}\; t\;\mathrm{d}A - \int_A \mathbf{f}\cdot\delta\mathbf{u}\;\mathrm{d}A. \tag{46}$$

To facilitate the numerical solution of the variational formulation, both linearization and discretization are required. The procedure adopted here largely follows the method presented in [19], ensuring consistency with established wrinkling models. The key aspects of the discretization process are outlined below. The formulation supports various types of basis functions, including classical Lagrange polynomials commonly used in standard finite element methods, as well as Non-Uniform Rational B-Splines (NURBS), which are frequently applied in isogeometric analysis (IGA). Due to their ability to represent geometry exactly and provide

higher-order continuity, NURBS have been widely adopted in structural analysis. A detailed discussion of their advantages can be found in [41,42].

The displacement field $\mathbf{u}$ is discretized as a linear combination of shape functions N^a and nodal displacement vectors $\mathbf{u}^a$:

$$\mathbf{u} = \sum_{a}^{n_{sh}} N^a \mathbf{u}^a, \tag{47}$$

where n_{sh} is the total number of shape functions. Each component u_i^a $(i = 1, 2, 3)$ corresponds to the displacement in the global x-, y-, and z-directions. To refer to the displacement components within a global degree of freedom index r, the mapping $r = 3(a-1)+i$ is adopted, such that $u_r = u_i^a$. Differentiation with respect to a displacement variable u_r yields:

$$\frac{\partial \mathbf{u}}{\partial u_r} = N^a \mathbf{e}_i, \tag{48}$$

where $\mathbf{e}_i$ denotes the global Cartesian base vectors. Taking the partial derivative of the virtual work expression in Eq. (46) with respect to u_r, leads to the residual force vector $\mathbf{R}$:

$$R_r = F_r^{\text{int}} - F_r^{\text{ext}} = \int_A \mathbf{S}_{\text{eff}} : \frac{\partial \mathbf{E}}{\partial u_r}\, t \;\mathrm{d}A - \int_A \mathbf{f} \cdot \frac{\partial \mathbf{u}}{\partial u_r}\,\mathrm{d}A, \tag{49}$$

where $\mathbf{F}^{\text{int}}$ and $\mathbf{F}^{\text{ext}}$ represent the internal and external nodal force vectors, respectively. By linearizing the residual vector defined in Eq. (49) with respect to u_s, we obtain the tangent stiffness matrix $\mathbf{K}$, which consists of internal and external components, denoted as $\mathbf{K}^{\text{int}}$ and $\mathbf{K}^{\text{ext}}$, respectively:

$$K_{rs} = K_{rs}^{\text{int}} - K_{rs}^{\text{ext}} = \int_A \left(\frac{\partial \mathbf{S}_{\text{eff}}}{\partial u_s} : \frac{\partial \mathbf{E}}{\partial u_r} + \mathbf{S}_{\text{eff}} : \frac{\partial^2 \mathbf{E}}{\partial u_r \partial u_s} \right) t \;\mathrm{d}A - \int_A \frac{\partial \mathbf{f}}{\partial u_s} \cdot \frac{\partial \mathbf{u}}{\partial u_r}\,\mathrm{d}A. \tag{50}$$

In the above, the derivative of the effective second Piola–Kirchhoff stress tensor with respect to u_s is given by:

$$\frac{\partial \mathbf{S}_{\text{eff}}}{\partial u_s} = \mathbb{C}_{\text{eff}} : \frac{\partial \mathbf{E}}{\partial u_s}. \tag{51}$$

As seen in the linearization, both the first and second derivatives of the Green–Lagrange strain tensor with respect to the displacement variables are required, and their detailed expressions can be found in [4].

When the external load $\mathbf{f}$ is independent of the displacement field, the external stiffness contribution $\mathbf{K}^{\text{ext}}$ vanishes. The linearized system at each iteration step is then given by:

$$\mathbf{K}\Delta\mathbf{u} = -\mathbf{R}, \tag{52}$$

where $\Delta\mathbf{u}$ is the displacement increment vector. The iterative process continues until the norm of the residual vector $\mathbf{R}$ falls below a predefined tolerance, thereby yielding the converged solution for the displacement field.

5. Numerical examples

This section assesses the accuracy of the proposed wrinkling model for hyperelastic materials through four numerical examples: inflation, stretching, simple shear and twisting. The results are compared against established reference data from the literature or high-order shell element analyses. Nonlinear static isogeometric analysis with NURBS basis functions is used. Unless stated otherwise, a degradation factor of $\eta = 0$ is applied in all simulations.

5.1. A square airbag under inflation-induced wrinkling

In the first example, we simulate the inflation of a square, isotropic membrane.

This benchmark problem was originally introduced by [43] for linear elastic materials and was later extended to hyperelastic membranes by [38,44]. As shown in Fig. 5, the square airbag has a side length of $L = \sqrt{1.2^2/2}\times 10^3$ mm and a thickness of $t = 0.1$ mm. The membrane is modeled using a compressible Neo-Hookean material, with the strain energy density function defined as:

$$\psi(\mathbf{C}) = \frac{\mu}{2}\left(J^{-2/3}\mathrm{tr}\,(\mathbf{C}) - 3\right) + \frac{K}{4}\left(J^2 - 1 - 2\ln J\right), \tag{53}$$

where the material parameters $\mu = \frac{E}{2(1+\nu)}$ and $K = \frac{E}{3(1-2\nu)}$ are determined by Young's modulus $E = 588$ MPa and Poisson's ratio $\nu = 0.4$. Owing to symmetry, only one-quarter of the structure is modeled. Symmetry boundary conditions are imposed along the internal edges Γ_3 and Γ_4, while displacements in the z-direction are constrained along the outer boundaries Γ_1 and Γ_2. The airbag is subjected to a gradually increasing pressure P, which acts normal to the membrane surface and reaches a final value of 5×10^{-3} MPa (note that $\mathbf{K}_{\text{ext}}$ is neglected). As discussed in previous studies, the application of pressure P on an initially flat membrane can lead to a singular stiffness matrix at the beginning of the simulation, making the problem numerically challenging. To circumvent this issue, dead loads are applied in the x- and y-directions along the edges Γ_1 and Γ_2 to pre-stretch the membrane. These loads are gradually reduced and completely removed as the pressure reaches its final value.

To facilitate comparison with previous studies, the proposed model is discretized using bi-linear membrane elements with mesh sizes ranging from 8×8 to 32×32, and a degradation factor $\eta = 1\times 10^{-3}$ is applied. As summarized in Table 1, four key quantities

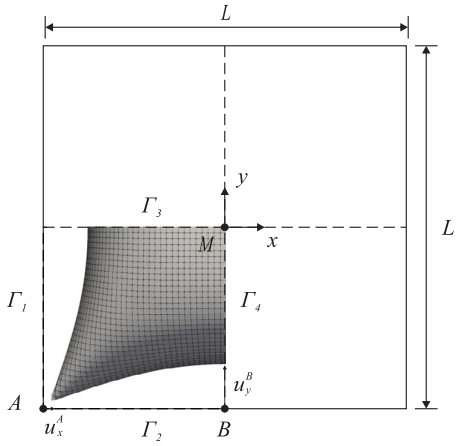

Fig. 5. Geometry and boundary conditions of an airbag under inflation pressure.

Table 1
Comparison of results from literature and present work (PW).

No. elements	5 × 5	25 × 25	8 × 8		16 × 16		32 × 32		16 × 16	32 × 32	64 × 64	128 × 128
	[44]		[38]	PW	[38]	PW	[38]	PW	KL-shell			
u_z^M (m)	0.2144	0.2245	0.2153	0.2246	0.2181	0.2245	0.2188	0.2244	0.2215	0.2229	0.2235	0.2244
u_x^A (m)	0.0265	0.0307	0.0357	0.0345	0.0333	0.0330	0.0315	0.0319	0.0283	0.0295	0.0303	0.0306
u_y^B (m)	0.1207	0.1158	–	0.1137	–	0.1141	–	0.1141	0.1096	0.1093	0.1116	0.1214
σ_1^M (MPa)	–	–	–	17.3	–	17.3	–	17.3	17.8	17.6	17.4	17.2

are evaluated at different mesh resolutions: the out-of-plane displacement at the membrane center (u_z^M), the vertical displacements at points A and B (u_x^A, u_y^B), and the first principal stress at point M (σ_1^M).

As shown in Table 1, the present results (PW) exhibit excellent agreement with both the finest-mesh data reported in [44] and the reference values from [38] across all tested mesh densities. Notably, even at the coarsest resolution of 8 × 8, the predicted central out-of-plane displacement u_z^M is already close to the reference solution obtained from a 128 × 128 bi-cubic KL-shell analysis. This suggests that the proposed model provides highly accurate results with significantly reduced computational effort. When the mesh is further refined, the evaluated quantities such as displacements and principal stresses match well with the KL-shell reference, further confirming the accuracy and robustness of the proposed wrinkling formulation.

5.2. A rectangular membrane under stretching-induced wrinkling

In the second example, we analyze the wrinkling behavior of a rectangular membrane subjected to uniaxial tensile loading. This example has attracted considerable attention [3,8–10,39,45,46] due to its characteristic behavior involving wrinkle formation at small strains, followed by restabilization at finite strain. The geometric configuration is shown in Fig. 6, where the membrane dimensions are $L = 280\,\text{mm}$, $W = 140\,\text{mm}$, and $t = 0.14\,\text{mm}$, corresponding to aspect ratios of $L/W = 2$ and $t/W = 10^{-3}$.

A uniform tensile displacement is applied to the right boundary in the x-direction, inducing a strain ε in the same direction. The left boundary is fixed to prevent rigid body motion. Due to symmetry, only a quarter of the membrane is modeled. The boundary conditions are imposed as follows: along the boundary Γ_1, symmetry is imposed by fixing displacements normal to the edge, i.e., $u_x = 0$. On Γ_2, an anti-symmetry condition is applied by constraining the displacements in y- and z-directions, in accordance with the modeling setup reported in [11]. The boundary Γ_3 left unconstrained. Along Γ_4, displacements in the y- and z-directions are fixed, while displacements in the x-direction are constrained to remain uniform across the boundary.

Following the comparison presented in [11], the membrane is modeled as a hyperelastic material governed by the incompressible Mooney–Rivlin constitutive law, which was shown to provide the best agreement with experimental data among several candidate models. The corresponding strain energy density function is defined as:

$$\psi_{el}(\mathbf{C}) = \frac{\mu_1}{2}\left(I_1 - 3\right) - \frac{\mu_2}{2}\left(I_2 - 3\right), \tag{54}$$

where $I_1 = \text{tr}(\mathbf{C})$ and $I_2 = \frac{1}{2}((\text{tr}(\mathbf{C}))^2 - \text{tr}(\mathbf{C}^2))$ are the invariants of $\mathbf{C}$, and the material parameters are set to $\mu_1 = 3.16 \times 10^5$ Pa and $\mu_2 = -1.24 \times 10^5$ Pa.

The stretching-induced wrinkling response is simulated using the proposed wrinkling model with meshes of 8 × 4 and 16 × 8 bi-linear elements. For reference and validation purposes, and following [47], the numerical results are compared with those obtained using a 32 × 32 bi-cubic Kirchhoff–Love shell mesh. As demonstrated in [47], this level of shell discretization yields predictions

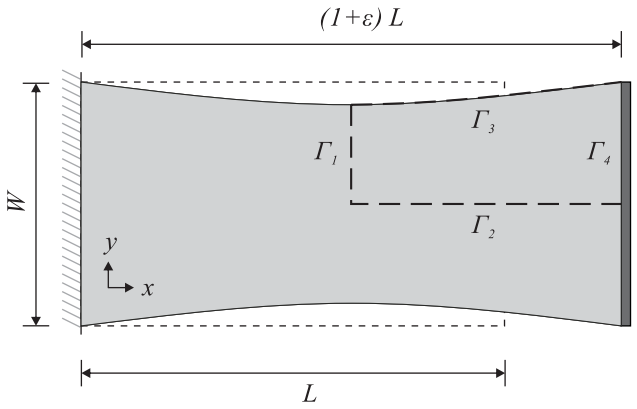

Fig. 6. Geometry and boundary conditions of a rectangular membrane under stretching.

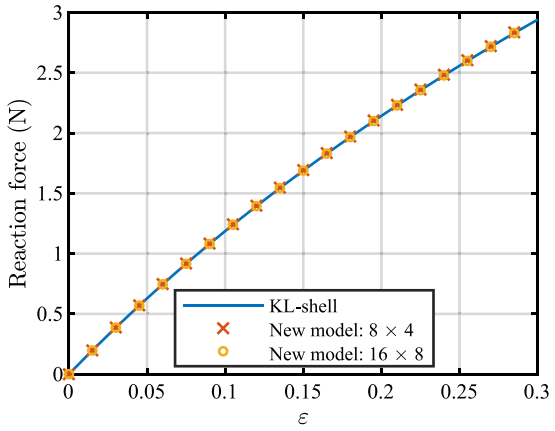

Fig. 7. Comparison of reaction forces between the KL-shell model and the new model under varying strain.

that are in good agreement with experimental results within the range of strains $\varepsilon \approx 0 - 0.3$, where most of the wrinkling occurs. Beyond this range, increasing deviations between the shell simulations and the experimental data were observed [11]. Consequently, the subsequent quantitative comparisons are restricted to this strain interval. For the Kirchhoff–Love shell reference solution, the nonlinear equilibrium path is traced using Crisfield's spherical arc-length method [48]. For the proposed membrane wrinkling model, the response is obtained using a standard Newton–Raphson iteration scheme.

Fig. 7 compares the reaction force–strain responses predicted by the Kirchhoff–Love shell reference and the proposed membrane model. An excellent agreement is observed over the entire range $0 \leq \varepsilon \leq 0.3$. Furthermore, the results obtained with the 8×4 and 16×8 meshes are nearly indistinguishable, demonstrating that with the proposed wrinkling model, a the coarse mesh with 8×4 is sufficient. In addition, the computational efficiency of the different models is assessed in terms of computational time. All simulations were performed on a computing cluster using a parallel pool of 12 workers. The reported times correspond to wall-clock time. The Kirchhoff–Love shell model requires approximately 13 184 s, whereas the proposed wrinkling model with a 8×4 mesh requires only 290 s. This corresponds to a reduction in computational time by a factor of approximately 45.5.

Fig. 8 shows the wrinkling pattern comparison between the KL-shell model and new model at three different strain levels (To accurately resolve the localization of the wrinkled region, a 32×32 mesh, consistent with the KL-shell simulations, is employed in this comparison). In this figure, red regions indicate wrinkled areas, whereas white regions correspond to taut zones predicted by the model. As the applied strain increases, the results show a progressive shortening of the wrinkling wavelength (see Fig. 9), indicating that the wrinkled region becomes more localized, which is also captured by the new model.

By definition, the membrane wrinkling model cannot provide information about the wrinkling amplitude. Therefore, for having another value for comparison, we compare the width of the wrinkled area according to the shell simulations and those with the new model. This width is measured at the bottom edge Γ_1, and the results are shown in Fig. 9.

For the Kirchhoff–Love shell solution, boundary points are classified as wrinkled if their out-of-plane displacement exceeds a prescribed threshold, with the threshold set to one-thirtieth of the maximum displacement amplitude ($\max(w)/30$, with $\max(w) \approx 0.429$ mm). The wrinkling width is then defined as the spatial extent of these points measured in the transverse (y) direction.

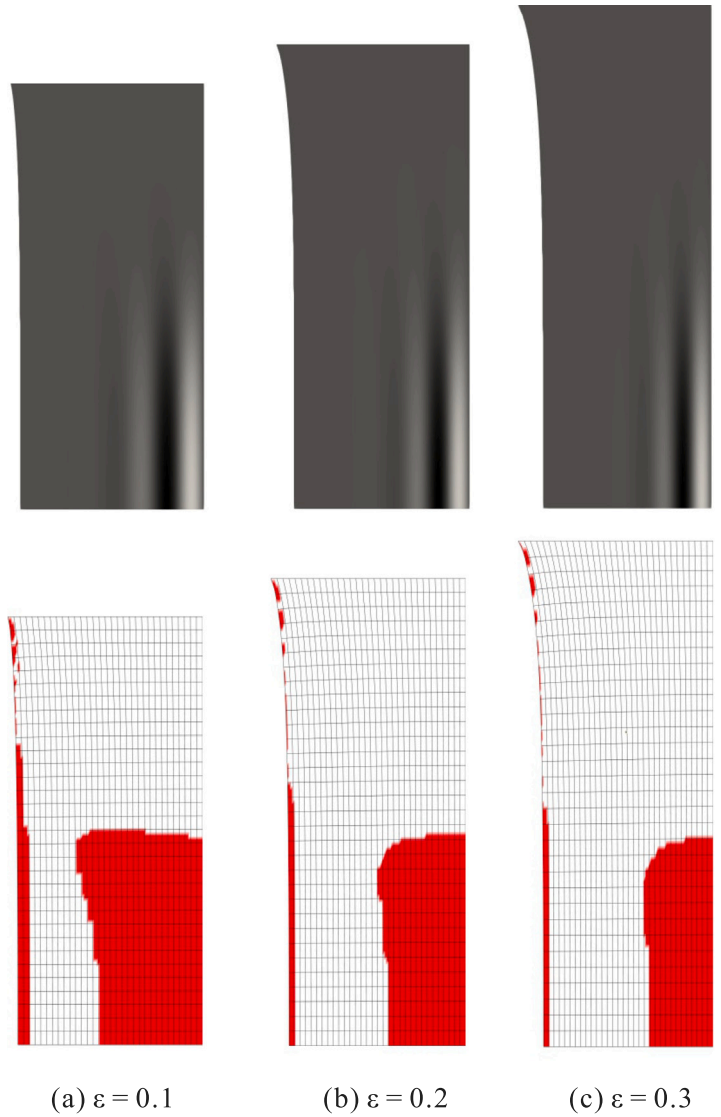

Fig. 8. Wrinkling evolution under increasing strain predicted by the KL-shell model (top) and new model (bottom). Red indicates wrinkled regions, while white indicates taut zones. (For interpretation of the references to color in this figure legend, the reader is referred to the web version of this article.)

For the Kirchhoff–Love shell model, the wrinkling width remains zero at the initial stage and starts to increase at about $\varepsilon \approx 0.025$, reaching a maximum value of approximately $40\,\mathrm{mm}$ at about $\varepsilon \approx 0.05$. With further stretching, the wrinkling width gradually decreases.

In contrast, the results of the new model (red curve) show a very large width of the wrinkled region at low strains, which suddenly drops at about $\varepsilon \approx 0.05$ and then matches very well with the results of the shell simulation. The reason for this is that in the beginning, there are large regions with very low compressive stresses, which are not sufficient to cause wrinkling in the shell model, but which are categorized as wrinkled according to tension field theory. This can also be directly observed in Fig. 8, where wrinkling appears near the boundaries in the new model. According to tension field theory and the mixed wrinkling criterion, regions are classified as wrinkled once the second principal stress becomes non-positive ($S_2 \leq 0$), while in reality, some compressive stress can be sustained. In our model, we do have the possibility to account for residual compressive stiffness through the degradation factor η introduced in (40). However, this does not change the results shown in Fig. 9, because the evaluation of the wrinkled area is done as a postprocessing step, using the assumption of tension field theory and the mixed wrinkling criterion. It is important to note that the observed discrepancy is purely a postprocessing issue and does not affect the predictive quality of the results for the global load-carrying behavior, as confirmed in Fig. 7. Nevertheless, this observation motivated us to modify the wrinkling criterion

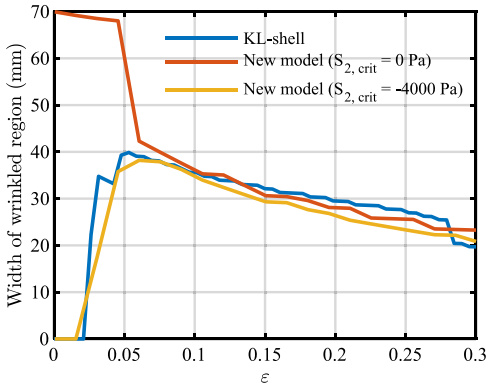

Fig. 9. Comparison of the width of the wrinkled region under increasing strain between the KL-shell model and the new models with different critical stress. The wrinkling width is measured along the boundary Γ_1 of the membrane.

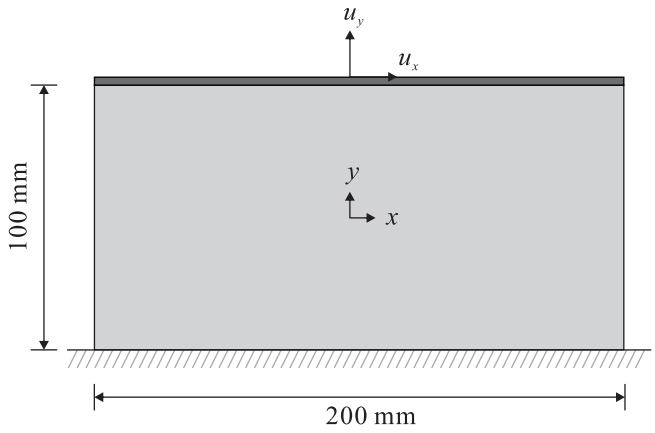

Fig. 10. Geometry and boundary conditions of a stretched rectangular membrane under shear.

just for this postprocessing step by introducing a critical compressive stress $S_{2,crit}$, such that wrinkling is identified for $S_2 < S_{2,crit}$. A systematic investigation of appropriate critical stress levels is out of the scope of the present paper, and an empirical approach for this example is chosen here. Fig. 7 depicts the results for $S_{2,\text{crit}} = -4000\,\text{Pa}$. The value is chosen such that the first occurrence of wrinkling is at a strain close to the one from the shell solution. As can be seen, this modified curve then matches very closely to the shell results across the entire range.

5.3. A rectangular membrane under simple shear-induced wrinkling

In the third example, we consider a rectangular membrane with dimensions 200 mm in length, 100 mm in width, and 0.2 mm in thickness, as shown in Fig. 10. Its hyperelastic behavior follows the formulation provided in [36], where the strain energy potential for plane stress is defined as

$$\psi(\mathbf{C}) = \frac{1}{2}\mu\left(\text{tr}\,(\mathbf{C}) - 2\right) - \frac{\lambda + 2\mu}{4}\left(2\log J + \log\left(\lambda + 2\mu\right) - \log\left(\lambda J^2 + 2\mu\right)\right), \tag{55}$$

where the material properties are expressed in terms of the Lamé constants, including $\lambda = 1852.07\,\text{N mm}^{-2}$ and $\mu = 207.90\,\text{N mm}^{-2}$. The loading procedure follows the methodology described in [36]. Initially, a small vertical displacement $u_y = 1\,\text{mm}$ is applied at the top boundary, while $u_x = 0\,\text{mm}$ remains fixed, introducing a minor tensile stretch. Subsequently, u_x is incrementally increased up to 10 mm, while $u_y = 1\,\text{mm}$ is held constant, leading to a predominantly shear-driven deformation.

Fig. 11 illustrates the shear force–displacement response of the membrane under the applied loading conditions. The simulation is performed using a 32×16 discretization with bi-linear quadrilateral elements. The plot compares the reaction force obtained from different models, including the reference wrinkling model in the literature [36], the standard membrane model (i.e., a classical membrane model without wrinkling treatment), and the newly proposed model. A key observation is that around $u_x = 2\,\text{mm}$, the reaction force curve exhibits a reduction in slope, indicating a decrease in stiffness. This phenomenon suggests the onset of wrinkling effects and is successfully captured by the reference model [36], as well as by the proposed model. In contrast, the classical membrane

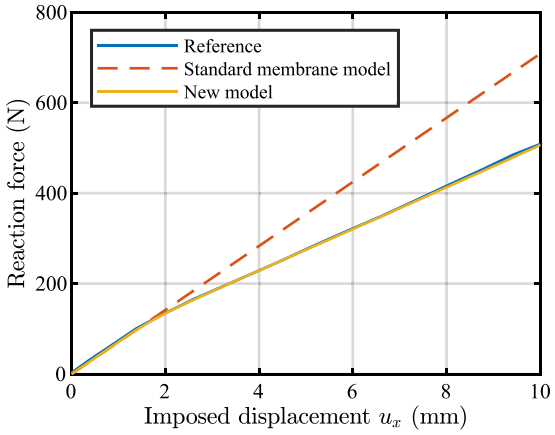

Fig. 11. Shear force–displacement response.

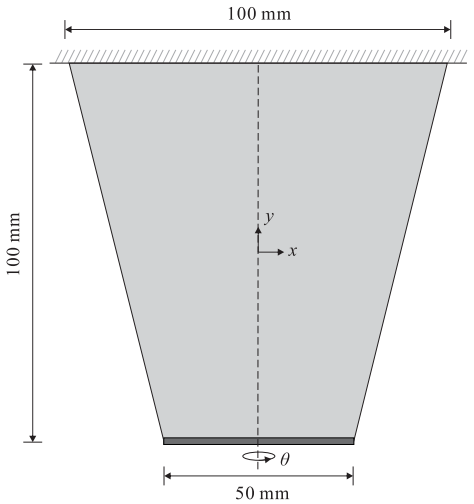

Fig. 12. Geometry and boundary conditions of a stretched membrane under twisting.

model does not exhibit this stiffness reduction; instead, it predicts a continuously increasing reaction force with a nearly constant slope, highlighting its inability to account for wrinkling effects. The close agreement of the new model with the reference solutions further demonstrates its capability to accurately capture the mechanical response of the membrane under shear loading.

5.4. A prestretched membrane under twisting-induced wrinkling

In the last example, we investigate the mechanical behavior of a membrane subjected to combined stretching and twisting, as illustrated in Fig. 12. The membrane initially has a trapezoidal shape with a top width of 100 mm, a bottom width of 50 mm, and a height of 100 mm. Its thickness is set to 5×10^{-3} mm. The material response is modeled using an incompressible Neo-Hookean hyperelastic law, with the strain energy density function defined as

$$\psi_{el}(\mathbf{C}) = \frac{\mu}{2}\left(I_1 - 3\right), \tag{56}$$

where μ is determined by Young's modulus $E = 1 \times 10^3$ MPa and Poisson's ratio $\nu = 0.5$. The boundary conditions are applied in two stages. The top edge is fully clamped, restricting all degrees of freedom. The bottom edge is first subjected to a downward displacement of 50 mm, driving the membrane into the finite strain regime. After stretching, The rotational deformation is imposed via a set of equivalent displacement boundary conditions, enabling the membrane to twist around its central axis. This loading condition triggers the formation and evolution of wrinkles as the rotation increases, as visualized in Fig. 14.

To generate a reference solution for model validation, the membrane is discretized using bi-cubic KL-shell elements with mesh densities of 16×16, 32×32 and 64×64. These simulations serve as a benchmark against which the performance of the proposed wrinkling model is assessed. Fig. 13 shows the relationship between the applied torque and the prescribed rotation. The torque

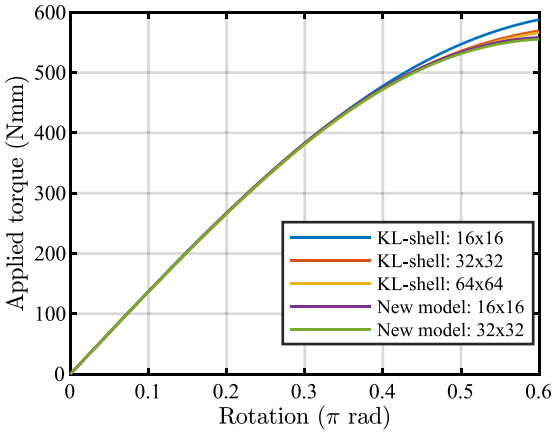

Fig. 13. Applied torque–rotation response.

increases nonlinearly with rotation, and the rate of increase gradually slows down. The applied torque is computed by integrating the internal force contributions multiplied by the corresponding rotational displacements at the loaded boundary. The results converge with increasing mesh density, indicating that the 64×64 KL-shell mesh provides a reliable reference solution. Comparisons are then made with the proposed wrinkling model, using bi-quadratic membrane elements. Remarkably, even with a coarse 16×16 mesh, the proposed model closely follows the KL-shell reference across the entire loading range. Minor deviations appear only at higher rotation. Overall, the results demonstrate that the proposed model captures the global torsional response with high accuracy, while offering a substantial reduction in computational cost compared to the shell-based formulation. In addition, the identification of the wrinkled regions closely matches the results obtained from the shell model, as illustrated in Fig. 14. In this visualization, the red regions represent wrinkled areas, while the white regions correspond to the taut zones predicted by our model. At $\theta = 0.3\pi$ (Fig. 14(a)), a narrow band of wrinkles begins to develop along the central axis of the membrane, while the regions near both ends remain in a taut state. As the rotation increases to $\theta = 0.4\pi$ (Fig. 14(b)), the wrinkled zone expands and starts to propagate toward the upper and lower boundaries. At $\theta = 0.5\pi$ (Fig. 14(c)), the wrinkling becomes more prominent and widespread, covering a substantial portion of the central domain. Finally, at $\theta = 0.6\pi$ (Fig. 14(d)), the wrinkled band extends across nearly the entire height of the membrane, leaving only narrow taut zones at the extremities.

6. Conclusion

In this paper, we introduced a novel wrinkling model for hyperelastic membranes that ensures variational consistency and numerical efficiency. The approach is formulated within the framework of spectral decomposition of the stress tensor and is capable of handling both compressible and incompressible materials under general three-dimensional constitutive laws. Unlike conventional methods that rely on case-specific logic to distinguish between taut, wrinkled, and slack regions, our model incorporates all membrane states into a unified formulation. A notable advantage of the proposed method lies in its compact stress formulation. This not only simplifies implementation but also improves computational performance without sacrificing accuracy. The performance of the proposed wrinkling model for hyperelastic membranes was evaluated using four representative benchmark examples, including inflation-induced out-of-plane loading, uniaxial stretching, simple shear, and twisting, to assess its predictive capability across a broad range of wrinkling behaviors. The simulation results show excellent agreement with established reference solutions, including those obtained from high-order Kirchhoff–Love shell formulations. Although the current implementation is based on an isogeometric framework, the proposed formulation is fully compatible with conventional finite element methods and can be readily integrated into standard FEM codes.

Future extensions of this work may include incorporating anisotropic material behavior and modeling dynamic wrinkling processes. These directions will further expand the scope and applicability of the proposed formulation in engineering applications.

CRediT authorship contribution statement

Daobo Zhang: Writing – original draft, Visualization, Validation, Software, Methodology, Investigation, Data curation, Conceptualization. **Josef Kiendl:** Writing – review & editing, Supervision, Resources, Methodology, Conceptualization.

Declaration of competing interest

The authors declare that they have no known competing financial interests or personal relationships that could have appeared to influence the work reported in this paper.

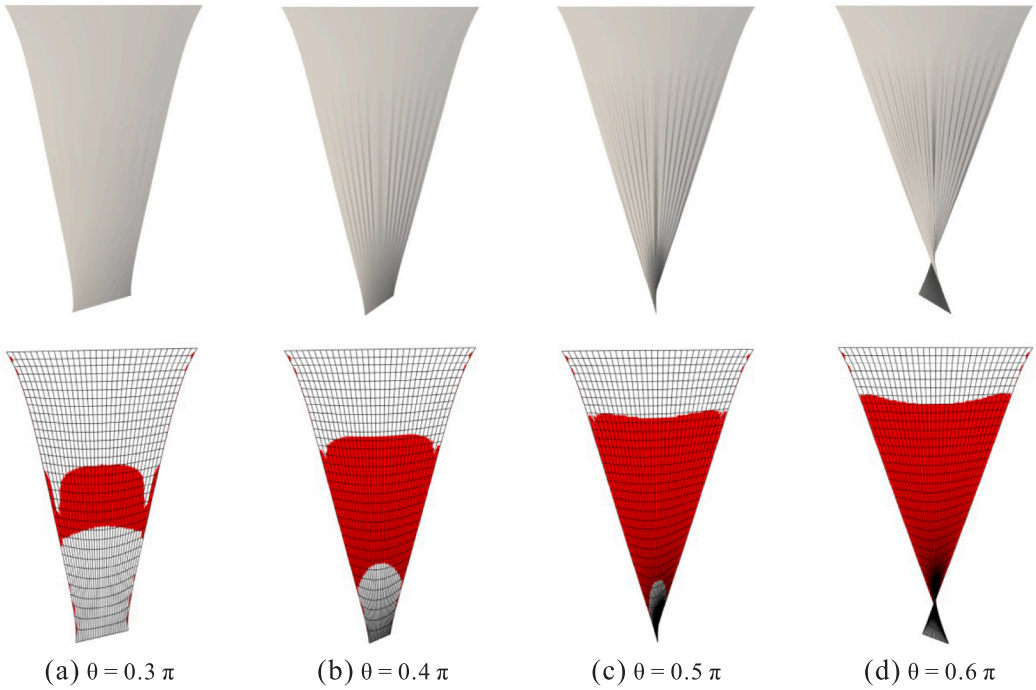

Fig. 14. Wrinkling evolution comparison under increasing rotation: KL-shell results (top) and new model (bottom). Red indicates wrinkled regions; white indicates taut zones. (For interpretation of the references to color in this figure legend, the reader is referred to the web version of this article.)

Appendix A. Simplification of the stress relation for linear elastic materials

Here, we demonstrate that in the case of linear elastic materials, the expression in Eq. (41) can be simplified accordingly. The constitutive tensor for plane stress linear elasticity is given by

$$\mathbb{C} = \left(\lambda - \frac{\lambda^2}{\lambda + 2\mu}\right) \mathbf{I} \otimes \mathbf{I} + 2\mu \mathbb{I} = \frac{E}{1-\nu^2} \left(\nu\, \mathbf{I} \otimes \mathbf{I} + (1-\nu)\, \mathbb{I}\right), \tag{A.1}$$

where the Lamé constants are defined as $\lambda = \frac{E\nu}{(1+\nu)(1-2\nu)}$ and $\mu = \frac{E}{2(1+\nu)}$. Here, E is Young's modulus, ν is Poisson's ratio, $\mathbf{I}$ denotes the second-order identity tensor, and $\mathbb{I}$ is the fourth-order identity tensor.

For isotropic materials, the relation $\mathbf{I} = \mathbf{M}_1 + \mathbf{M}_2$ holds, and due to orthogonality, we have

$$\mathbf{I} : \mathbf{M}_2 = (\mathbf{M}_1 + \mathbf{M}_2) : \mathbf{M}_2 = 1. \tag{A.2}$$

Accordingly, the relevant contractions are

$$\mathbb{C} : \mathbf{M}_2 = \frac{E}{1-\nu^2} \left(\nu\, \mathbf{I} + (1-\nu)\, \mathbf{M}_2\right), \quad \mathbf{M}_2 : \mathbb{C} : \mathbf{M}_2 = \frac{E}{1-\nu^2}. \tag{A.3}$$

Finally, we obtain

$$\mathbf{M}_2 + \left(-\frac{1}{\mathbf{M}_2 : \mathbb{C} : \mathbf{M}_2}\right) \mathbb{C} : \mathbf{M}_2 = \mathbf{M}_2 - \nu\, \mathbf{M}_1 - \nu\, \mathbf{M}_2 + (\nu - 1)\, \mathbf{M}_2 = -\nu\, \mathbf{M}_1. \tag{A.4}$$

Appendix B. Derivatives with respect to the Cauchy deformation tensor

We provide the expressions for the derivatives $\partial S_2/\partial \mathbf{C}$, $\partial \mathbf{M}_2/\partial \mathbf{C}$, and $\partial \mathbb{C}/\partial \mathbf{C}$, as referenced in Eqs. (36)–(38).

For $\partial S_2/\partial \mathbf{C}$, the derivative of a scalar function with respect to the Cauchy deformation tensor $\mathbf{C}$ can be expressed using the chain rule and the principal stretches λ_i, following [49]:

$$\frac{\partial S_2}{\partial \mathbf{C}} = \frac{\partial S_2}{\partial \lambda_i^2} \frac{\partial \lambda_i^2}{\partial \mathbf{C}} = \frac{1}{2\lambda_i} \frac{\partial S_2}{\partial \lambda_i} \mathbf{M}_i, \tag{B.1}$$

where $i = 3$ for compressible materials and $i = 2$ for incompressible materials. For compressible materials, $\partial S_2/\partial \lambda_i$ can be obtained directly from the derivative of the strain energy function. For incompressible materials, the expression is more involved and follows

the formulation given in [39]:

$$\frac{\partial S_\alpha}{\partial \lambda_\beta} = \frac{1}{\lambda_\alpha}\left[\frac{\partial^2 \psi_{el}}{\partial \lambda_\alpha \partial \lambda_\beta} - \frac{1}{\lambda_\beta}\left(\lambda_3 \frac{\partial^2 \psi_{el}}{\partial \lambda_3 \partial \lambda_\alpha} + \delta^3_\alpha \frac{\partial \psi_{el}}{\partial \lambda_3}\right) - \frac{1}{\lambda_\alpha}\left(\lambda_3 \frac{\partial^2 \psi_{el}}{\partial \lambda_3 \partial \lambda_\beta} + \delta^3_\beta \frac{\partial \psi_{el}}{\partial \lambda_3}\right) - \lambda_3 \frac{\partial \psi_{el}}{\partial \lambda_3}\frac{(1-\delta^\beta_\alpha)}{\lambda_\alpha \lambda_\beta} - \delta^\beta_\alpha \frac{1}{\lambda_\alpha}\left(\frac{\partial \psi_{el}}{\partial \lambda_\alpha} - \frac{1}{\lambda_\alpha}\lambda_3 \frac{\partial \psi_{el}}{\partial \lambda_3}\right)\right]. \tag{B.2}$$

where δ^j_i is the Kronecker delta and ψ_{el} denotes the strain energy density of the hyperelastic material.

For $\partial \mathbf{M}_2/\partial \mathbf{C}$, the derivative of the eigenprojector with respect to the Cauchy deformation tensor $\mathbf{C}$ can be evaluated using the expression given in [50]:

$$\mathbb{M}_i = \frac{\partial \mathbf{M}_i}{\partial \mathbf{C}} = \frac{1}{2(\lambda_i - \lambda_j)}(\mathbb{G}_{ij} + \mathbb{G}_{ji}), \quad i \neq j, \tag{B.3}$$

with

$$\mathbb{G}^{ijkl}_{mn} = M^{ik}_m M^{jl}_n + M^{il}_m M^{jk}_n. \tag{B.4}$$

Finally, the sixth-order tensor $\mathbb{D} = \partial \mathbb{C}/\partial \mathbf{C}$ can be evaluated using standard tensor calculus, as noted in [51]. Alternatively, it may be approximated using finite differences. While it is possible to neglect the term involving $\mathbb{D}$, doing so compromises the asymptotically quadratic convergence of the Newton–Raphson method.

Data availability

Data will be made available on request.

References

[1] L. Zheng, Wrinkling of dielectric elastomer membranes, California Institute of Technology, 2009.
[2] V. Nayyar, K. Ravi-Chandar, R. Huang, Stretch-induced stress patterns and wrinkles in hyperelastic thin sheets, Int. J. Solids Struct. 48 (25–26) (2011) 3471–3483.
[3] T.J. Healey, Q. Li, R.-B. Cheng, Wrinkling behavior of highly stretched rectangular elastic films via parametric global bifurcation, J. Nonlinear Sci. 23 (2013) 777–805.
[4] J. Kiendl, M.-C. Hsu, M.C. Wu, A. Reali, Isogeometric Kirchhoff–Love shell formulations for general hyperelastic materials, Comput. Methods Appl. Mech. Engrg. 291 (2015) 280–303.
[5] D.J. Steigmann, A well-posed finite-strain model for thin elastic sheets with bending stiffness, Math. Mech. Solids 18 (1) (2013) 103–112.
[6] M. Taylor, K. Bertoldi, D.J. Steigmann, Spatial resolution of wrinkle patterns in thin elastic sheets at finite strain, J. Mech. Phys. Solids 62 (2014) 163–180.
[7] M. Taylor, B. Davidovitch, Z. Qiu, K. Bertoldi, A comparative analysis of numerical approaches to the mechanics of elastic sheets, J. Mech. Phys. Solids 79 (2015) 92–107.
[8] C. Fu, H.-H. Dai, F. Xu, Computing wrinkling and restabilization of stretched sheets based on a consistent finite-strain plate theory, Comput. Methods Appl. Mech. Engrg. 384 (2021) 113986.
[9] Q. Li, T.J. Healey, Stability boundaries for wrinkling in highly stretched elastic sheets, J. Mech. Phys. Solids 97 (2016) 260–274.
[10] C. Fu, T. Wang, F. Xu, Y. Huo, M. Potier-Ferry, A modeling and resolution framework for wrinkling in hyperelastic sheets at finite membrane strain, J. Mech. Phys. Solids 124 (2019) 446–470.
[11] H.M. Verhelst, M. Möller, J.H. Den Besten, A. Mantzaflaris, M.L. Kaminski, Stretch-based hyperelastic material formulations for isogeometric Kirchhoff–Love shells with application to wrinkling, Computer-Aided Des. 139 (2021) 103075.
[12] A.A. Sipos, E. Fehér, Disappearance of stretch-induced wrinkles of thin sheets: a study of orthotropic films, Int. J. Solids Struct. 97 (2016) 275–283.
[13] F. Liu, F. Xu, C. Fu, Orientable wrinkles in stretched orthotropic films, Extrem. Mech. Lett. 33 (2019) 100579.
[14] Y. Yang, C. Fu, F. Xu, A finite strain model predicts oblique wrinkles in stretched anisotropic films, Internat. J. Engrg. Sci. 155 (2020) 103354.
[15] C. Fu, Y. Yang, T. Wang, F. Xu, A consistent finite-strain plate model for wrinkling of stretched anisotropic hyperelastic films, Thin-Walled Struct. 179 (2022) 109643.
[16] E. Reissner, On tension field theory, in: Proc. of the 5th Int. Congr. for Applied Mechanics Harvard Univ. & MIT, 1938, pp. 88–92.
[17] K. Nakashino, M.C. Natori, Efficient modification scheme of stress-strain tensor for wrinkled membranes, AIAA J. 43 (1) (2005) 206–215.
[18] X. Liu, C.H. Jenkins, W.W. Schur, Large deflection analysis of pneumatic envelopes using a penalty parameter modified material model, Finite Elem. Anal. Des. 37 (3) (2001) 233–251.
[19] D. Zhang, J. Kiendl, A variationally consistent membrane wrinkling model based on spectral decomposition of the strain tensor, Comput. Methods Appl. Mech. Engrg. 432 (2024) 117386.
[20] D. Zhang, J. Kiendl, A variationally consistent membrane wrinkling model based on spectral decomposition of the strain and stress tensors, J. Mech. Phys. Solids (2025) 106331.
[21] Y. Miyazaki, Wrinkle/slack model and finite element dynamics of membrane, Internat. J. Numer. Methods Engrg. 66 (7) (2006) 1179–1209.
[22] C. Liu, Q. Tian, D. Yan, H. Hu, Dynamic analysis of membrane systems undergoing overall motions, large deformations and wrinkles via thin shell elements of ANCF, Comput. Methods Appl. Mech. Engrg. 258 (2013) 81–95.
[23] S. Kang, S. Im, Finite element analysis of dynamic response of wrinkling membranes, Comput. Methods Appl. Mech. Engrg. 173 (1–2) (1999) 227–240.
[24] A. Jarasjarungkiat, R. Wüchner, K.-U. Bletzinger, A wrinkling model based on material modification for isotropic and orthotropic membranes, Comput. Methods Appl. Mech. Engrg. 197 (6–8) (2008) 773–788.
[25] D.G. Roddeman, J. Drukker, C.W.J. Oomens, J.D. Janssen, The wrinkling of thin membranes: part I—theory, J. Appl. Mech. 54 (4) (1987) 884–887.
[26] M. Epstein, On the wrinkling of anisotropic elastic membranes, J. Elasticity 55 (1999) 99–109.
[27] S. Kang, S. Im, Finite element analysis of wrinkling membranes, J. Appl. Mech. 64 (2) (1997) 263–269.
[28] R.K. Miller, J.M. Hedgepeth, An algorithm for finite element analysis of partly wrinkled membranes, AIAA J. 20 (12) (1982) 1761–1763.

[29] P. Contri, B. Schrefler, A geometrically nonlinear finite element analysis of wrinkled membrane surfaces by a no-compression material model, Commun. Appl. Numer. Methods 4 (1) (1988) 5–15.
[30] K. Woo, H. Igawa, C. Jenkins, Analysis of wrinkling behavior of anisotropic membrane, Comput. Model. Eng. Sci. 6 (2004) 397–408.
[31] R. Rossi, M. Lazzari, R. Vitaliani, E. Oñate, Simulation of light-weight membrane structures by wrinkling model, Internat. J. Numer. Methods Engrg. 62 (15) (2005) 2127–2153.
[32] T. Akita, K. Nakashino, M. Natori, K. Park, A simple computer implementation of membrane wrinkle behaviour via a projection technique, Internat. J. Numer. Methods Engrg. 71 (10) (2007) 1231–1259.
[33] A. Jarasjarungkiat, R. Wüchner, K.-U. Bletzinger, Efficient sub-grid scale modeling of membrane wrinkling by a projection method, Comput. Methods Appl. Mech. Engrg. 198 (9–12) (2009) 1097–1116.
[34] H. Le Meitour, G. Rio, H. Laurent, A. Lectez, P. Guigue, Analysis of wrinkled membrane structures using a plane stress projection procedure and the dynamic relaxation method, Int. J. Solids Struct. 208 (2021) 194–213.
[35] A.C. Pipkin, Relaxed energy densities for large deformations of membranes, IMA J. Appl. Math. 52 (3) (1994) 297–308.
[36] J. Mosler, A novel variational algorithmic formulation for wrinkling at finite strains based on energy minimization: application to mesh adaption, Comput. Methods Appl. Mech. Engrg. 197 (9–12) (2008) 1131–1146.
[37] A. Niewiarowski, S. Adriaenssens, R.M. Pauletti, A conic programming approach to the wrinkling of pneumatic membranes using convex potentials, Comput. Struct. 292 (2024) 107231.
[38] H.M. Verhelst, M. Möller, J.H. Den Besten, A wrinkling model for general hyperelastic materials based on tension field theory, Comput. Methods Appl. Mech. Eng. 441 (2025) 117955.
[39] H.M. Verhelst, M. Möller, J. Den Besten, A. Mantzaflaris, M.L. Kaminski, Stretch-based hyperelastic material formulations for isogeometric Kirchhoff–Love shells with application to wrinkling, Computer-Aided Des. 139 (2021) 103075.
[40] T. Iwasa, M. Natori, K. Higuchi, Evaluation of tension field theory for wrinkling analysis with respect to the post-buckling study, J. Appl. Mech. 71 (4) (2004) 532–540.
[41] J.A. Cottrell, T.J. Hughes, Y. Bazilevs, Isogeometric analysis: toward integration of CAD and FEA, John Wiley & Sons, 2009.
[42] T.J. Hughes, J.A. Cottrell, Y. Bazilevs, Isogeometric analysis: CAD, finite elements, NURBS, exact geometry and mesh refinement, Comput. Methods Appl. Mech. Engrg. 194 (39–41) (2005) 4135–4195.
[43] N. Bauer, Zur Darstellung von Falten in Membranen mit hilfe der methode der finiten elemente, in: Mitteilungen / UniversitÄt Stuttgart, Sonderforschungsbereich 64, SFB 64, Weitgespannte FlÄchentragwerke ; 33, SFB 64, Stuttgart, 1975.
[44] A. Diaby, C. Wielgosz, et al., Buckling and wrinkling of prestressed membranes, Finite Elem. Anal. Des. 42 (11) (2006) 992–1001.
[45] T. Wang, C. Fu, F. Xu, Y. Huo, M. Potier-Ferry, On the wrinkling and restabilization of highly stretched sheets, Internat. J. Engrg. Sci. 136 (2019) 1–16.
[46] A. Panaitescu, M. Xin, B. Davidovitch, J. Chopin, A. Kudrolli, Birth and decay of tensional wrinkles in hyperelastic sheets, Phys. Rev. E 100 (5) (2019) 053003.
[47] H.M. Verhelst, A. Mantzaflaris, M. Möller, J.H. Den Besten, Goal-adaptive meshing of isogeometric Kirchhoff–Love shells, Eng. Comput. (2024) 1–28.
[48] M. Crisfield, An arc-length method including line searches and accelerations, Internat. J. Numer. Methods Engrg. 19 (9) (1983) 1269–1289.
[49] G.A. Holzapfel, Nonlinear solid mechanics: a continuum approach for engineering science, 2002.
[50] C. Miehe, M. Lambrecht, Algorithms for computation of stresses and elasticity moduli in terms of Seth–Hill's family of generalized strain tensors, Commun. Numer. Methods Eng. 17 (5) (2001) 337–353.
[51] R. Kruse, N. Nguyen-Thanh, L. De Lorenzis, T.J. Hughes, Isogeometric collocation for large deformation elasticity and frictional contact problems, Comput. Methods Appl. Mech. Engrg. 296 (2015) 73–112.